

## Article

# Rapid Microwave Synthesis of $\beta$ -SnWO<sub>4</sub> Nanoparticles: An Efficient Anode Material for Lithium Ion Batteries

H. N. Sumedha<sup>1</sup>, Mabkhoot A. Alsaieri<sup>2,3</sup> , Mohammed S. Jalalah<sup>2,4</sup>, M. Shashank<sup>1,5</sup>, Fahad A. Alharthi<sup>6,\*</sup>, Naushad Ahmad<sup>6</sup>, Jari S. Algethami<sup>3</sup>, Vishwanth Vishwanth<sup>7</sup> and Nagaraju Ganganagappa<sup>1,\*</sup>

- <sup>1</sup> Energy Materials Research Laboratory, Department of Chemistry, Siddaganga Institute of Technology, Tumakuru 572103, India; hnsumedha@gmail.com (H.N.S.); mshashank95@gmail.com (M.S.)
- <sup>2</sup> Promising Center for Sensors and Electronic Devices (PCSED), Advanced Materials and Nano Research Center, Najran University, P.O. Box 1988, Najran 11001, Saudi Arabia; mabkhoot.alsaieri@gmail.com (M.A.A.); jalalah@gmail.com (M.S.J.)
- <sup>3</sup> Chemistry Department, Faculty of Science and Art at Sharurah, Najran University, Sharurah 68342, Saudi Arabia; jery\_s@hotmail.com
- <sup>4</sup> Department of Electrical Engineering, Faculty of Engineering, Najran University, Najran, P.O. Box 1998, Najran 11001, Saudi Arabia
- <sup>5</sup> Department of Studies and Research in Industrial Chemistry, School of Chemical Sciences, Kuvempu University, Shankaragatta 577451, India
- <sup>6</sup> Department of Chemistry, College of Science, King Saud University, P.O. Box 2455, Riyadh 11451, Saudi Arabia; anaushad@ksu.edu.sa
- <sup>7</sup> Department of Chemistry, Jyothi Institute of Technology, Bangalore 560082, India; vishwahosur@gmail.com
- \* Correspondence: fharthi@ksu.edu.sa (F.A.A.); nagarajugn@sit.ac.in (N.G.)



**Citation:** Sumedha, H.N.; Alsaieri, M.A.; Jalalah, M.S.; Shashank, M.; Alharthi, F.A.; Ahmad, N.; Algethami, J.S.; Vishwanth, V.; Ganganagappa, N. Rapid Microwave Synthesis of  $\beta$ -SnWO<sub>4</sub> Nanoparticles: An Efficient Anode Material for Lithium Ion Batteries. *Crystals* **2021**, *11*, 334. <https://doi.org/10.3390/cryst11040334>

Academic Editors: Ahmad Umar, Sotirios Baskoutas and Nikolaos Bouropoulos

Received: 26 February 2021  
Accepted: 23 March 2021  
Published: 26 March 2021

**Publisher's Note:** MDPI stays neutral with regard to jurisdictional claims in published maps and institutional affiliations.



**Copyright:** © 2021 by the authors. Licensee MDPI, Basel, Switzerland. This article is an open access article distributed under the terms and conditions of the Creative Commons Attribution (CC BY) license (<https://creativecommons.org/licenses/by/4.0/>).

**Abstract:** We report a facile synthesis of  $\beta$ -SnWO<sub>4</sub> nanoparticles via a microwave heat treatment using SnCl<sub>2</sub> and H<sub>2</sub>WO<sub>4</sub> in the presence of tamarind seed powder. An X-ray diffraction analysis confirmed a crystalline nature revealing a cubic structure of  $\beta$ -SnWO<sub>4</sub> nanoparticles. The morphological features were visualized using a scanning electron microscope that exhibited homogeneously distributed clusters of nanoparticles, which were further confirmed using a transmission electron microscope. The micrographs also displayed some porosity. Energy dispersive X-ray spectroscopy confirmed the elemental contents such as tin, oxygen and tungsten in the same stoichiometric ratio as expected by the respective empirical formula. A high-resolution transmission electron microscope was used to find the *d*-spacing, which was ultimately used to analyze the structural parameters. The spectrum obtained using Fourier transform infrared spectroscopy illuminated different stretching vibrations. Additionally, a Barrett–Joyner–Halenda analysis was carried out to investigate the N<sub>2</sub> adsorption-desorption isotherm as well as to govern the pore size distribution. Cyclic voltammetry measurements were implemented to analyze the ongoing electrode reactions throughout the charge/discharge for the  $\beta$ -SnWO<sub>4</sub> nanostructures. The galvanometric charge/discharge curves for  $\beta$ -SnWO<sub>4</sub> are also discussed. A high specific capacitance (600 mAhg<sup>-1</sup> at 0.1 C) and excellent columbic efficiency (~100%) were achieved.

**Keywords:** Li-ion battery; anode;  $\beta$ -SnWO<sub>4</sub> NPs; microwave

## 1. Introduction

The demand of energy storage devices with enhanced capabilities has increased manifold in the 21st century. In this context, researchers worldwide are looking for such devices and materials that might lead the scientific community to cope with energy storage needs by designing and developing innovative resources. In the current era, energy renovation is at the forefront of research [1]. Lithium-ion batteries (LIBs) are considered to be promising because of their high power density, life cycle and gravimetric and volumetric energy along with long self-discharge properties. Therefore, LIBs are still unbeaten in the energy storage industry [2]. Meanwhile, the earth's crust has a limited availability of lithium resources and

their use is beyond the limits. Consequently, they are becoming costly [3,4]. Alternatively, batteries are facing various problems including storage capacity and chemical stability [5]. Additionally, its specific capacity is extremely low, i.e.,  $372 \text{ mAhg}^{-1}$ . To resolve such issues, there is a need to investigate other favorable electrode materials exhibiting promising specific capacities and chemical stabilities. In the realm of rechargeable LIBs, various nanomaterials are under discussion as potential electrode materials.

Historically, LIBs have shown a massive intensification through two decades in specific energy values ranging from 90 to  $250 \text{ mAhg}^{-1}$  [6]. In this regime, there have been many breakthroughs in energy storage devices (as electrode materials) due to the advancement in the field of nanomaterials [7–11]. Nanomaterials have exceptionally attractive physical and chemical properties; hence, they are reflected as being suitable for energy storage devices. The use of single metal oxides including  $\text{TiO}_2$  [12],  $\text{SnO}_2$  [13] and  $\text{Ta}_2\text{O}_5$  [14] has led to a loss in capacity with cycling. A literature survey reveals a good electrochemical performance of  $\beta\text{-SnWO}_4$  nanoparticles. These nanoparticles also offer an excellent diffusion of  $\text{Li}^+$  ions along exceptional cyclic stability as well as a high capacity. Furthermore, they are widely utilized as anode materials, for water splitting, for photodynamic tumor therapy, for humidity sensing and photocatalytic degradation, for example. Various routes have been adopted for the synthesis of  $\text{SnWO}_4$  including hydrothermal synthesis [15], a combustion method and a microwave method [16]. Initially, the gas sensing properties as well as the phase structure of  $\alpha$ - and  $\beta\text{-SnWO}_4$  were reported by Solis and Lantoo by employing different spectroscopic techniques [16,17]. Ede et al. adopted microwave synthesis to prepare  $\text{SnWO}_4$  [16]. Warmuth et al. employed a microwave assisted method to synthesize  $\beta\text{-SnWO}_4$  nanoparticles [18]. Furthermore, the photoelectrochemical properties of  $\beta\text{-SnWO}_4$  nanomaterials were analyzed by Cho et al. [19].  $\text{ZnWO}_4$  nanocrystals/reduced graphene oxide hybrids were prepared by Wang Xiao et al. via a facile hydrothermal route that revealed a performance of  $477 \text{ mAhg}^{-1}$  after 40 cycles [6].  $\alpha\text{-SnWO}_4$ /reduced graphene oxide nanoparticles were synthesized by Renkun Huang et al. through a facile single step hydrothermal reaction exhibiting a capacity of  $500 \text{ mAhg}^{-1}$  after 20 cycles [20].

The search for the finest electrode material for LIBs with a high capacity and that can easily be diffused into  $\text{Li}^+$  ions along with an increased life cycle is still under investigation. Owing to the promising features associated with  $\beta\text{-SnWO}_4$  nanoparticles and their wide utilization in energy storage applications, here we report a facile synthesis based on a rapid microwave heat treatment by the reaction of  $\text{SnCl}_2$  and  $\text{H}_2\text{WO}_4$  in the presence of tamarind seed powder. We present a detailed analysis of the electrochemical performance for potential use as an electrode material in LIBs. The material owed an exceptional specific capacitance ( $600 \text{ mAhg}^{-1}$  at 0.1 C) and a remarkable columbic efficiency nearly approaching 100% was achieved.

## 2. Experiment

### 2.1. Synthesis of $\beta\text{-SnWO}_4$ Nanoparticles

$\beta\text{-SnWO}_4$  nanoparticles were prepared through a rapid microwave heat treatment by the reaction of tin (II) chloride ( $\text{SnCl}_2$ ) and tungstic acid ( $\text{H}_2\text{WO}_4$ ) in the presence of tamarind seed powder. A typical procedure involved the addition of 220 mg of  $\text{SnCl}_2$  and 249 mg of  $\text{H}_2\text{WO}_4$  in a clean and dried crucible. In the meantime, 220 mg of tamarind seed powder was also added followed by the addition of 10 mL of distilled water. The obtained blend was stirred for about 10 min. At that time, the crucible was kept in a microwave oven at 900 W for 5 min. The resultant product was taken out of the oven and allowed to cool to room temperature naturally. It was then ground in a clean dried mortar and calcined at  $700 \text{ }^\circ\text{C}$  for 4 h under static air. A schematic of the sample synthesis is presented in Figure 1.

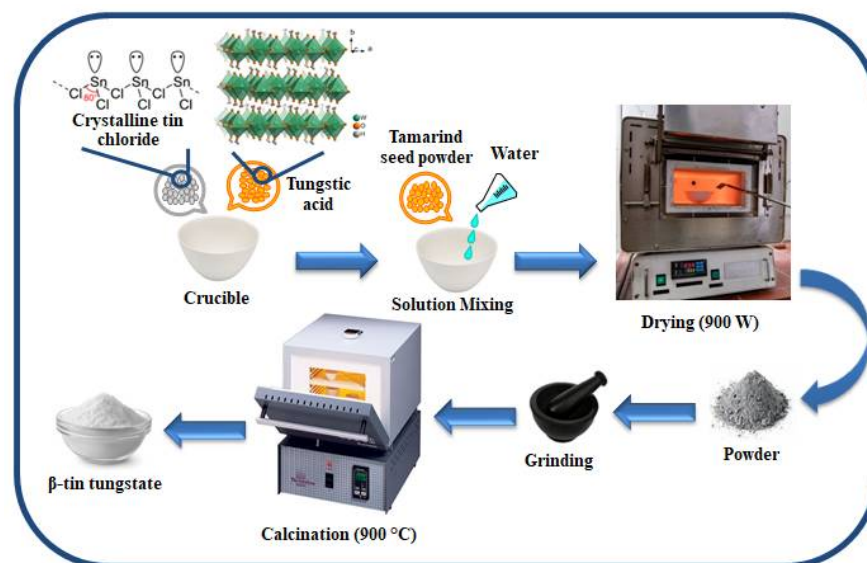


Figure 1. Schematic illustration of the sample synthesis.

## 2.2. Characterization

A Rigaku's (Tokyo, Japan) Smart Lab X-ray diffractometer (XRD) with Cu- $K_{\alpha}$  radiations ( $\lambda = 1.5406 \text{ \AA}$ ) was used to determine the crystalline nature and the confirmation of the phase. The molecular vibrations and structures of the materials were analyzed from  $350\text{--}4000 \text{ cm}^{-1}$  using a Bruker (Billerica, Massachusetts, United States) Alpha-P Fourier transforms infrared (FTIR) spectrometer by the KBr pellet method. JEOL(Tokyo, Japan)-JCM-6000 Plus scanning electron microscopy (SEM) and JEOL-JEM-2100 transmission electron microscopy (TEM) were utilized to observe the morphological features, particle size and structural parameters of  $\beta\text{-SnWO}_4$  nanoparticles, respectively. Using a Quanta chrome Nova 2200E-BET (surface area analyzer), the pore size and surface area were determined.

## 2.3. Electrode Fabrication for the Lithium Ion Battery

A coin cell was made to examine the electrochemical performance of  $\beta\text{-SnWO}_4$  nano-materials by fabricating it on a copper foil. The slurry was prepared by mixing the active materials ( $\beta\text{-SnWO}_4$  nanoparticles), PVDF (polyvinylidene fluoride) and acetylene black using a weight ratio of 80:5:15, respectively, using a few drops of N-methyl pyrrolidine as a solvent. The prepared slurry was uniformly coated on a Cu foil and subsequently dried at  $100 \text{ }^{\circ}\text{C}$  for 12 h in a vacuum oven. During the coil cell fabrication, a polypropylene membrane (Celgard-2400) was utilized as a separator. LiPF<sub>6</sub> (1M) dissolved in ethylene carbonate, dimethyl carbonate and diethyl carbonate (2:2:1) was used as an electrolyte. Cyclic voltammetry (CV) and galvanostatic charge-discharge (GCD) studies were recorded using a Bio-logic BCS 805 battery system. The CV measurements were performed in the voltage window from 0.01 to 3 V at a 50 mV/s scan rate. The voltage range of 0.01–3 V was also applied during the GCD analysis.

## 3. Results and Discussion

The XRD pattern of the sample was recorded in the  $2\theta$  range of  $15\text{--}70^{\circ}$ , as shown in Figure 2a. The existence of intensity peaks corresponding to the (200), (020), (001), (100), ( $-112$ ), (202), (411), (222), (112), (212), (211), (322), (820) and (811) planes was perfectly matched with JCPDS (Joint Committee on Powder Diffraction Standards) reference no. 01-070-1497 [16], a characteristic reference pattern of  $\beta\text{-SnWO}_4$ . It confirmed the wolframite-type cubic crystal structure of the sample, having space group no. 198 and a space group category of P-213 [21]. There were no extra peaks signifying the phase purity of the sample [18]. Further, the magnified image of a few peaks was illustrated to

differentiate between these peaks (Figure 2b). The lattice parameter ( $a$ ) was calculated from following equation:

$$a = \frac{\lambda \sqrt{h^2 + k^2 + l^2}}{2 \sin \theta_B} \quad (1)$$

The lattice parameter was measured to be  $a = b = c = 7.298 \text{ \AA}$ , resulting in a unit cell volume of  $388.697 \text{ \AA}^3$ . The average crystallite size ( $D_{hkl}$ ) was determined using Scherrer's formula as described by Equation (2) [22]:

$$D = \frac{k\lambda}{\beta \cos \theta_B} \quad (2)$$

where  $\beta$  was line broadening termed as full width at half maximum (FWHM),  $\theta_B$  represented Bragg's angle,  $\lambda$  was the wavelength with a value of  $1.54 \text{ \AA}$  and  $k = 0.9$ , the shape factor. The crystallite size as evaluated by this formula was  $28.63 \text{ nm}$ .

The crystallite size of the as-synthesized samples was also calculated using the Williamson–Hall (W–H) method as given by Equation (3) [23]:

$$\beta \cos \theta = k\lambda/D + 4\epsilon \sin \theta \quad (3)$$

where  $\epsilon$  represented the lattice strain. Figure 3 indicates the W–H plot of  $\beta\text{-SnWO}_4$  plotted between  $4\sin\theta$  at the  $x$ -axis and  $\beta\cos\theta$  along the  $y$ -axis. The  $D$  was measured from the  $y$ -intercept and depicted to be  $24.32 \text{ nm}$  while  $\epsilon$  measured the slope of the linear fit and was measured to be  $7.2 \times 10^{-2}$ . The linear fit of the W–H plot was expected to be a straight line parallel to  $x$ -axis but in the manifestation of  $\epsilon$  it gave a non-zero slope [24]. The measured crystallite size ( $24.32 \text{ nm}$ ) from the W–H plot was in close agreement with Scherrer's formula ( $28.63 \text{ nm}$ ).

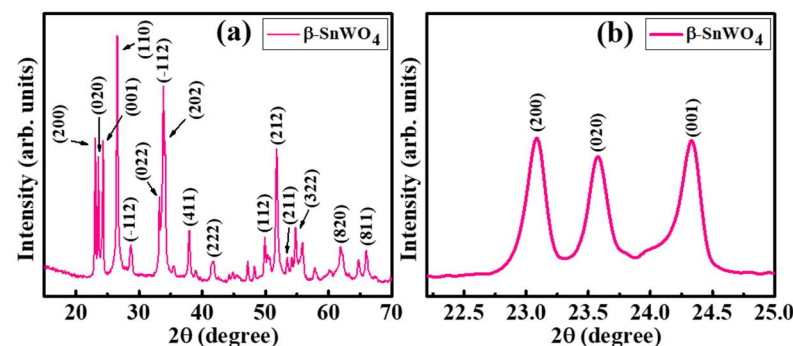


Figure 2. (a) Indexed X-ray diffractometer (XRD) pattern and (b) magnified image of certain peaks of  $\beta\text{-SnWO}_4$  nanoparticles.

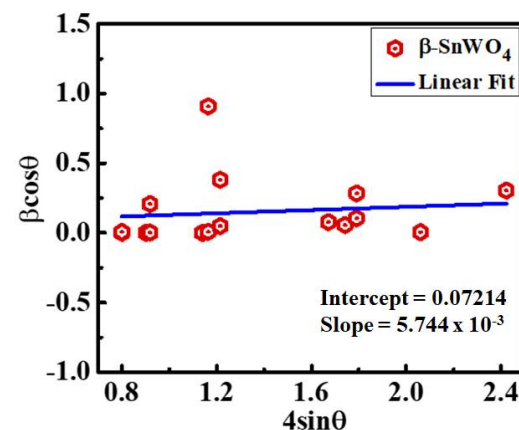


Figure 3. Williamson–Hall (W–H) plot of  $\beta\text{-SnWO}_4$  nanoparticles.

The accurate phase analysis and quantitative phase measurement of  $\beta$ -SnWO<sub>4</sub> were determined through a Rietveld refinement analysis via X'pert HighScore (Worcestershire, UK) Plus software. Figure 4 shows the well fitted XRD pattern of  $\beta$ -SnWO<sub>4</sub> at the same positions as prescribed in Figure 2. No significant phase transformation was perceived attributing the pure phase formation of the specimen. The structural reliability was evaluated by measuring R-factors such as the R-profile ( $R_p$ ), the R-expected ( $R_{exp}$ ), the R-profile ( $R_{wp}$ ) and the R-Bragg ( $R_B$ ) as well through the following Equations [25]:

$$R_{wp} = \left[ \frac{\sum_i w_i (I_c - I_o)}{\sum_i w_i I_o^2} \right]^{1/2} \quad (4)$$

$$R_{exp} = \left[ \frac{N - P}{\sum_i w_i I_o^2} \right]^{1/2} \quad (5)$$

$$R_{Bragg} = \frac{\sum |I(0) - I(c)|}{\sum |I(0)|} \quad (6)$$

$$R_p = \frac{\sum |I(0_i) - I(c_i)|}{\sum |I(0_i)|} \quad (7)$$

Here,  $P$  and  $N$  represented the number of refined parameters and the number of experimentally observed points and  $I_o$  and  $I_c$  presented the observed and calculated integrated intensities, respectively. Accordingly,  $w_i$  was the illustrating weight factor at  $i$  point of the diffraction profile and the goodness of fit ( $\chi^2$ ) was measured using Equation (8), given as [25]:

$$\chi^2 = \frac{R_{wp}}{R_{exp}} \quad (8)$$

The measured parameters from a Rietveld refinement analysis are summarized in Table 1. The obtained smaller value of  $\chi^2$  depicted the pure phase development of  $\beta$ -SnWO<sub>4</sub>.

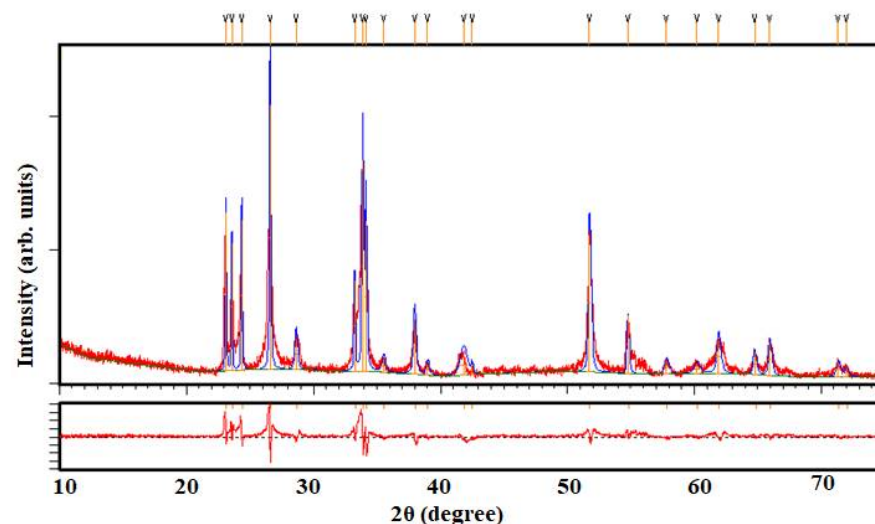
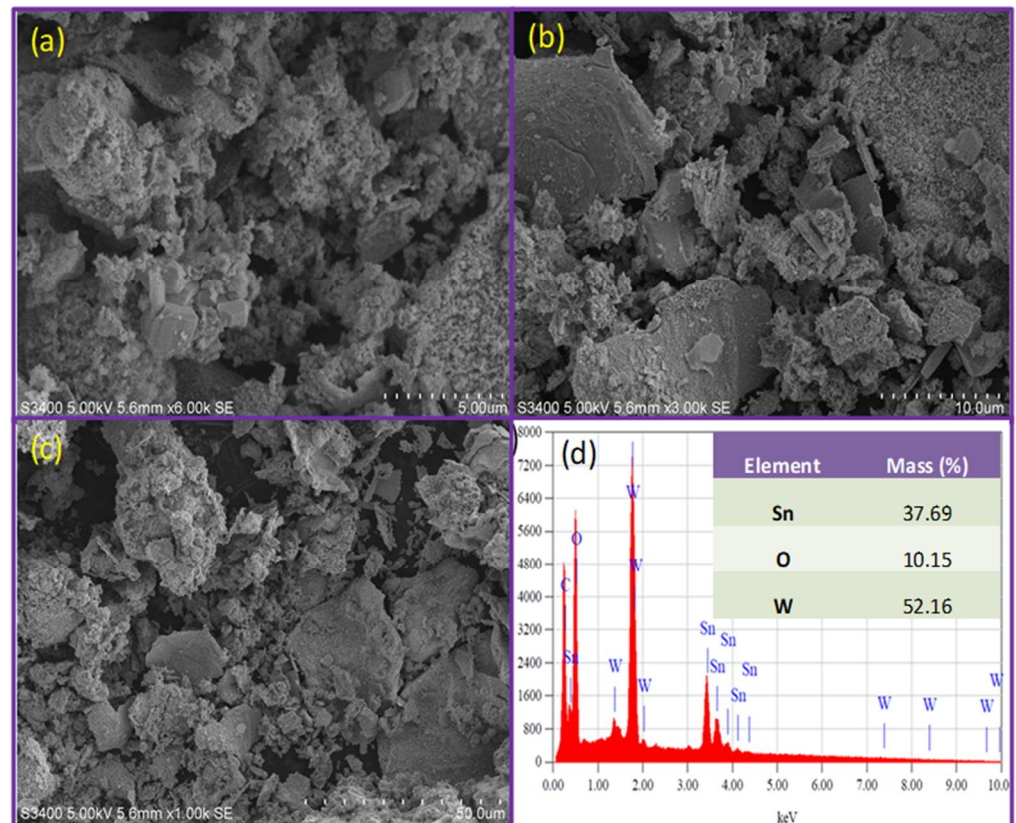


Figure 4. Rietveld refined XRD pattern of  $\beta$ -SnWO<sub>4</sub> nanostructures.

Table 1. Data obtained through Rietveld refinement of the diffraction data of  $\beta$ -SnWO<sub>4</sub>.

$R_{exp}$	$R_p$	$R_{wp}$	$D_{statics}$	Wt. $D_{statics}$	$\chi^2$
10.84	13.73	18.04	0.44	0.56	2.77

The SEM images for  $\beta$ -SnWO<sub>4</sub> are illustrated in Figure 5a–c. The micrographs were obtained at diverse magnifications revealing the formation of  $\beta$ -SnWO<sub>4</sub> nanoclusters along with a few sorts of layered and rough structures as well. Stone-like arbitrary and amalgamated particles of various sizes and shapes could be perceived in the micrographs. Figure 5b,c illustrates some rock-like structures along with very small particles. Furthermore, the images also revealed the porosity present in the samples.



**Figure 5.** (a–c) SEM images and (d) EDX spectrum (inset: elemental composition) of  $\beta$ -SnWO<sub>4</sub> nanoparticles.

The EDX spectrum of  $\beta$ -SnWO<sub>4</sub> was profiled (Figure 5d). It confirmed the existence of all of the constituent elements such as tin, oxygen and tungsten in the sample. The table shown in an inset of Figure 5d demonstrates the mass percentages of all of the elements.

The morphology of  $\beta$ -SnWO<sub>4</sub> was also examined using TEM and high resolution transmission electron microscope (HR-TEM) to obtain a detailed breakdown of the structures and to determine the interlayer *d*-spacing. Figure 6a,b illustrates the TEM images obtained at different magnifications. The micrographs profiled almost spherical shaped particles accompanied by some amalgamation. Further, a few pores could also be professed in the micrographs. The interlayer *d*-spacing was examined through HR-TEM and found to be 0.33 nm [24] and can be seen in Figure 6c. The lattice fringes of the (001) lattice plane of a wolframite-type cubic crystal structure  $\beta$ -SnWO<sub>4</sub> could be perceived (Figure 5d) as sketched by a selected area electron diffraction (SEAD) pattern. The occurrences of bright rings in the concerning pattern illustrated the company of highly crystallite particles. The existence of the lattice plane was in good agreement with the XRD pattern.

The FTIR spectrum for  $\beta$ -SnWO<sub>4</sub> was recorded in the range of 350–4000 cm<sup>−1</sup>, as shown in Figure 7. The peak appearing around 609 cm<sup>−1</sup> demonstrated an asymmetric stretching vibration of the WO<sub>6</sub><sup>−6</sup> group [24,26]. In the same way, the peaks emerging at 768 and 851 cm<sup>−1</sup> illuminated the stretching vibrations of the W–W and W–O–W bridging bonds [26]. The structural vibrations of the C–C or C–O–C bonds were in agreement with the peak occurring at 1443 cm<sup>−1</sup>. Further, the existence of a strong peak at 1640 cm<sup>−1</sup>

and a broad peak at 3421 corresponded with the stretching and bending vibrations of the hydroxyl (–OH) group. The symmetric stretching vibration of the C–H bond could be observed from the peak befalling at 2921  $\text{cm}^{-1}$ . The co-existence of all of the stretching and vibrational peaks confirmed the formation of the  $\beta\text{-SnWO}_4$  structure [27].

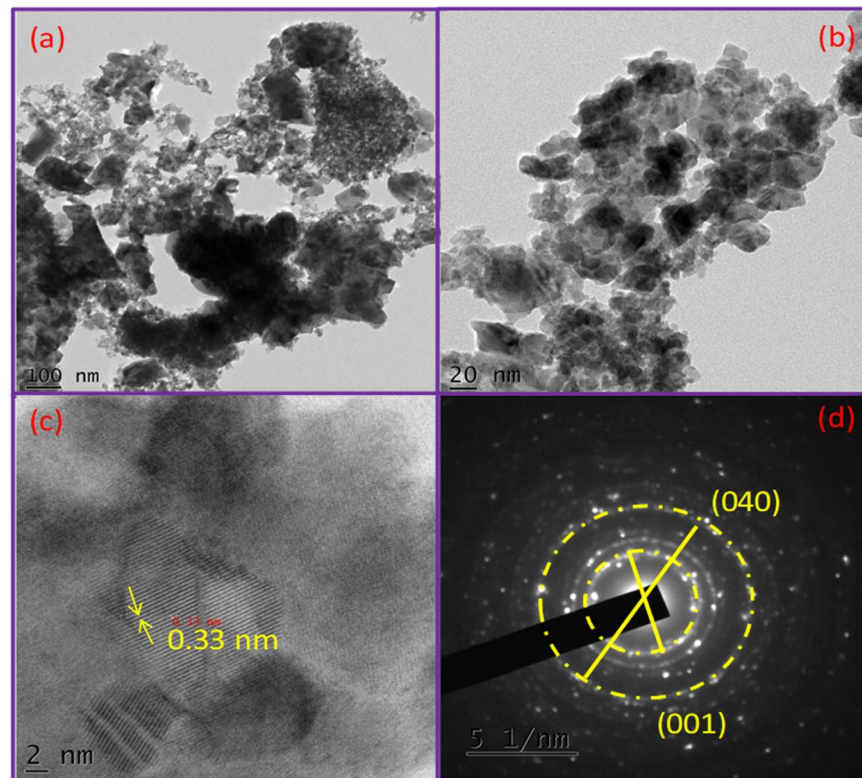


**Figure 6.** (a,b) TEM, (c) HR-TEM and (d) selected area electron diffraction (SEAD) pattern of  $\beta\text{-SnWO}_4$  nanoparticles.

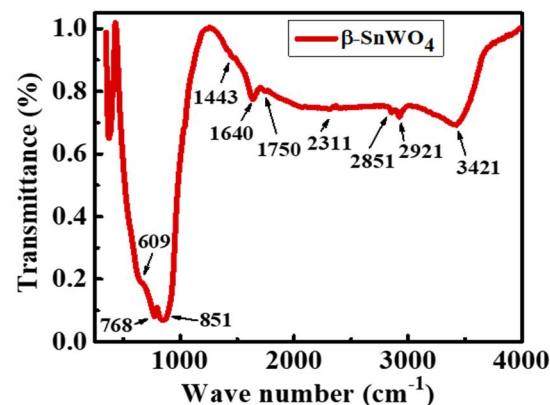


**Figure 7.** Fourier transforms infrared (FTIR) spectrum of  $\beta\text{-SnWO}_4$  nanoparticles.

A Barrett–Joyner–Halenda (BJH) analysis was carried out to investigate the  $\text{N}_2$  adsorption-desorption isotherm as well as to determine the pore size distribution. The curve sketched in Figure 8a clearly offered a desorption hysteresis of a type-IV isotherm curve [28,29] obtained under a relative pressure ( $P/P_0$ ) of 0.1–1.0. The characteristics of the mesostructured materials could be well explained on the basis of sharp capillary condensation steps occurring between the relative pressure intervals of 0.40–0.95. It also perceived an irregularity of mesopores in the product. The BJH pore size distribution is profiled in Figure 8b. A sharp peak could be depicted in the beginning of the distribution curve demonstrating an

average pore diameter of 3.35 nm. The pore volume and surface area of the particles in the sample were determined using a Brunauer–Emmett–Teller (BET) analysis. Accordingly, due to its plentiful range of pore diameters (2–80 nm), it could accumulate a higher number of charge carriers thus improving the electrolyte performance of the current specimen. Hence, it can offer its utilization in a wide collection of potential applications.

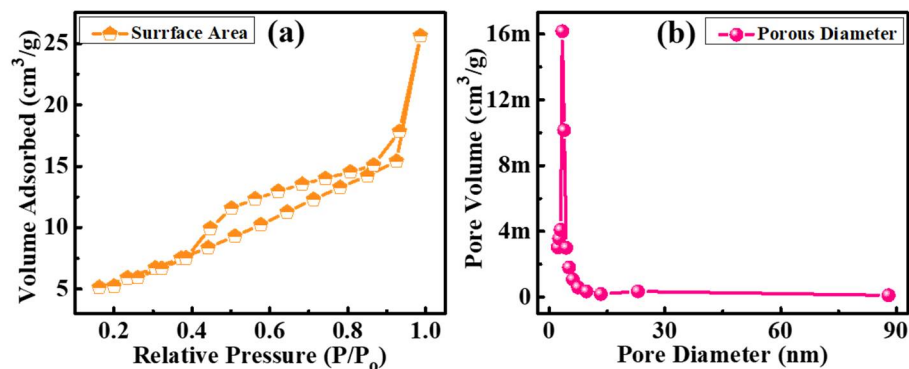
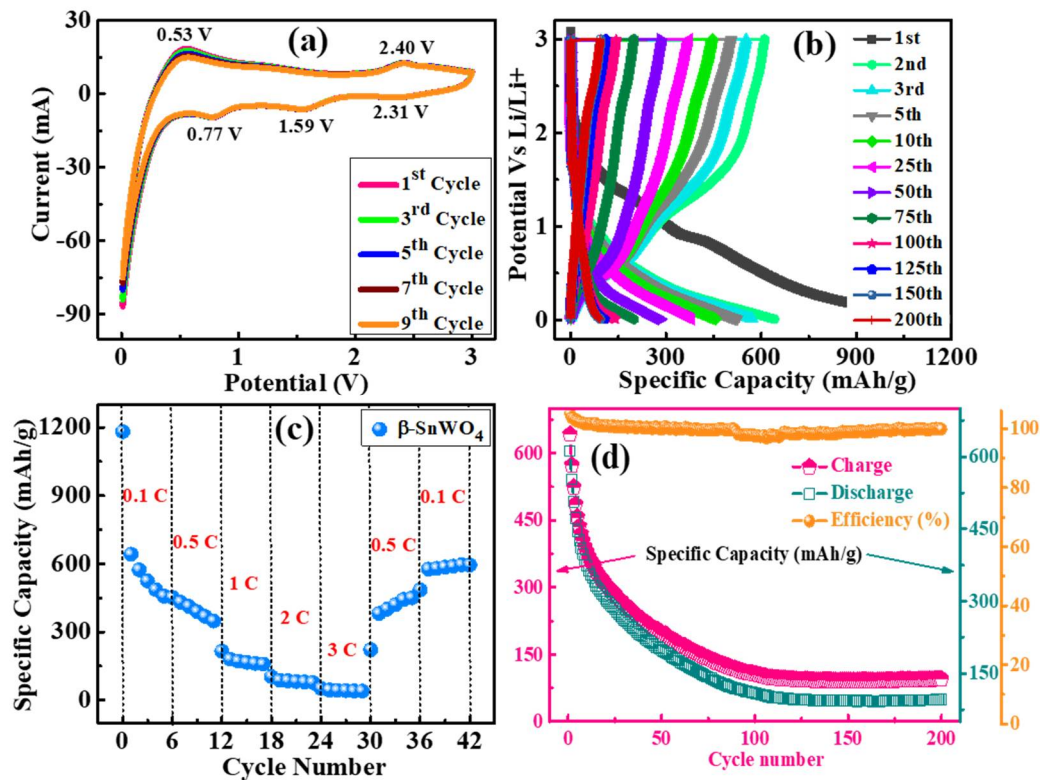


Figure 8. (a) Barrett–Joyner–Halenda (BJH) adsorption-desorption isotherm and (b) pore size distribution of  $\beta$ -SnWO<sub>4</sub> nanostructures.

CV measurements were implemented to analyze the ongoing electrode reactions throughout the charge/discharge for the  $\beta$ -SnWO<sub>4</sub> nanostructures. The CV profile was mapped under various current cycles and a potential window of 0.01 to 3.0 V and is demonstrated in Figure 9a. The composition clearly described the actuality of the anodic/cathodic peaks. Similar current humps could be perceived from all of the current cycles. During lithiation, three peaks could be depicted specifying a multi-lithiation progression [21]. The reduction of  $\beta$ -SnWO<sub>4</sub> to Sn and W was noticed from the first reduction peak and appeared around 2.31 V as prescribed in Equation (9). Another reduction peak occurred at 1.59 V justifying the Sn-metal reaction in the excess vicinity of the Li<sup>+</sup> ions (alloying reaction) [30]. The following reaction could be perceived in Equation (10). In addition, the W-metal reaction with LiSn and excessive Li<sup>+</sup> ions could be observed in Equation (11) that resulted from the existence of a third reduction peak at around 0.77 V. The reverse of the reduction known as oxidation also occurred. The anodic peak that appeared around 0.53 V was attributed to the de-alloying of Li<sub>x</sub>Sn while the peak that appeared at 2.40 V identified the oxidation of Sn and W to  $\beta$ -SnWO<sub>4</sub>. The probable electrochemical reactions were as follows [21]:



The galvanometric charge/discharge (GCD) curves for  $\beta$ -SnWO<sub>4</sub> at a scan rate of 0.1 C and in the voltage range of 0.01–3.0 V can be seen in Figure 9b. The first cycle exhibited a discharge capacity of 1180 mAhg<sup>-1</sup> and the second cycle displayed charge and discharge capacities of 608 mAhg<sup>-1</sup> and 638 mAhg<sup>-1</sup>, respectively. Theoretically,  $\beta$ -SnWO<sub>4</sub> demonstrates a capacity of 850 mAhg<sup>-1</sup> [26]. The excessive discharge capacity is mainly due to interfacial storage [31]. As the curves depicted a higher discharge capacity than charge capacity, this could be attributable to factors such as electrolyte decomposition, unavoidable solid electrolyte interface (SEI) formation and the generation of Li<sub>2</sub>O owing to irreversible Li-ion interactions [12]. A decrease in the charge/discharge capacities with an increase in the current rate represented an excellent ionic and electrical conductivity and an exceptional rate capability.



**Figure 9.** (a) Cyclic voltammogram, (b) galvanostatic charge-discharge, (c) rate capability at different current density and (d) cycling performance and coulombic efficiency of  $\beta$ -SnWO<sub>4</sub> nanoparticles.

The rate capability of  $\beta$ -SnWO<sub>4</sub> was examined at numerous current rates (0.1–3 C) and is shown in Figure 9c. A specific capacity of 54 mAhg<sup>-1</sup> was attained at a current rate of 3 C. Further, an excessive specific capacitance of 600 mAhg<sup>-1</sup> was noticeable when the reverse current was brought at 0.1 C. The contemporary extreme electrochemical performance of  $\beta$ -SnWO<sub>4</sub> indicates a highly stable electrode material towards energy storage applications. Table 2 illustrates a comparative study of the specific capacities of pure  $\beta$ -SnWO<sub>4</sub> and for various dopants.

**Table 2.** Comparative study of specific capacities along different C-rates for pure  $\beta$ -SnWO<sub>4</sub> and for other dopants.

Composition	Synthesis Method	C-Rates	Specific Capacity (mAhg <sup>-1</sup> )	References
$\beta$ -SnWO <sub>4</sub> -rGO	Solution combustion method followed by a low temperature hydrothermal method	0.1 C	578	[21]
$\beta$ -SnWO <sub>4</sub>	~	0.1 C	271	[21]
$\beta$ -SnWO <sub>4</sub> -rGO	~	3 C	165	[21]
$\beta$ -SnWO <sub>4</sub>	~	3 C	35	[21]
$\beta$ -SnWO <sub>4</sub>	Rapid microwave heat treatment	0.1 C	600	Current work
$\beta$ -SnWO <sub>4</sub>	~	3 C	54	Current work

The specific charge-discharge capacities and coulombic efficiency of  $\beta$ -SnWO<sub>4</sub> were performed at a C/10 rate and are profiled in Figure 9d. From the graph it was evident that almost constant and stabilized charge-discharge capacities of 105 and 58 mAhg<sup>-1</sup> were obtained. In addition, a coulombic efficiency of nearly 100% was professed.

The kinetic behaviors specifying the charge transfer properties of the as-synthesized electrodes were examined by means of a powerful electrochemical impedance spectroscopy

(EIS) tool. The EIS measurements were obtained before and after CD cycles and a Nyquist plot was sketched (illustrated in Figure 10) using a Randles circuit model (inset Figure 10). The outcome of the graph was a slope line in the low frequency region signifying an electron diffusion process and a semicircle arc in the high frequency region attributing the charge transfer resistance ( $R_{ct}$ ) [32]. The  $R_{ct}$  could be indicated from the radius of the semicircle at the electrolyte/electrode interface. The formation of semicircles of two different diameters indicated different  $R_{ct}$  values. The  $R_{ct}$  value for  $\beta$ -SnWO<sub>4</sub> after CD was much lower (108  $\Omega$ ) than that of before CD (163  $\Omega$ ) characterizing the presence of negative charges on the  $\beta$ -SnWO<sub>4</sub> surface. It thus hosted an electrostatic repulsion between the electrolyte/electrode boundaries leading to a low rate charge transfer [32].

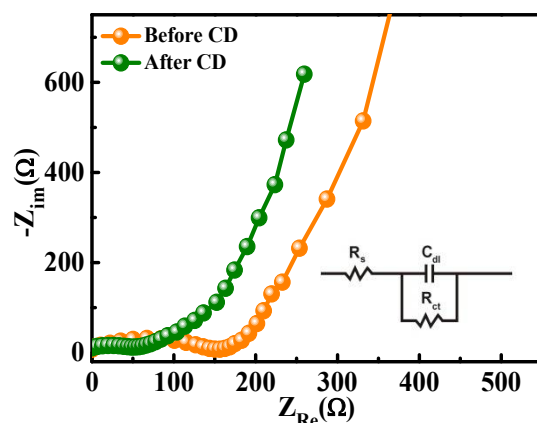


Figure 10. Nyquist plot for electrochemical impedance spectroscopy for  $\beta$ -SnWO<sub>4</sub>. CD = charge-discharge.

#### 4. Conclusions

$\beta$ -SnWO<sub>4</sub> nanoparticles were synthesized by a microwave heat treatment method facilitated by the reaction of SnCl<sub>2</sub> and H<sub>2</sub>WO<sub>4</sub> in the presence of tamarind seed powder. An XRD analysis confirmed the crystalline nature of  $\beta$ -SnWO<sub>4</sub> nanoparticles, which were found to be cubic in nature. A SEM analysis revealed the formation of  $\beta$ -SnWO<sub>4</sub> stone-like arbitrary and amalgamated nanoclusters with some traces of porosity. An EDX analysis confirmed the existence of all constituent elements, i.e., tin, oxygen and tungsten, in the desired stoichiometric ratio. Spherical shaped particles were perceived by TEM analysis and an interlayer *d*-spacing was examined through HR-TEM, which was found to be 0.33 nm corresponding to a (001) plane. The occurrence of bright rings in the pattern illustrated the highly crystallite nature of the sample. The peaks emerging in the FTIR spectrum at about 609, 768, 851 and 1443 cm<sup>-1</sup> illuminated the stretching vibrations of the WO<sub>6</sub><sup>-6</sup> group, the W–W and W–O–W bridging bonds and the C–C or C–O–C bonds, respectively. The irregularity of the mesopores in the product was perceived by a BJH analysis. A sharp peak as evident in the beginning of distribution curve demonstrated an average pore diameter of 3.35 nm. The CV profile was mapped under various current cycles, which confirmed the composition by describing the actuality of the anodic/cathodic peaks (multi-lithiation and de-lithiation processes). The reduction peak appearing around 2.31, 1.59 and 0.77 V demonstrated the reduction of  $\beta$ -SnWO<sub>4</sub> to Sn and W and the Sn-metal reaction and W-metal reaction, respectively. In the GCD analysis, the first cycle exhibited a discharge capacity of 1180 mAhg<sup>-1</sup> and the second cycle displayed charge and discharge capacities of 608 and 638 mAhg<sup>-1</sup>, respectively. Moreover, a decrease in charge/discharge capacities was observed with an increase in the current rate that represented excellent ionic and electrical conductivity and an exceptional rate capability of about 600 mAhg<sup>-1</sup> at 0.1 C (reverse current). In addition, it also exhibited ~100% columbic efficiency. The EIS measurements owed a high resistance for  $\beta$ -SnWO<sub>4</sub> before CD (163  $\Omega$ ) than that of after CD (108  $\Omega$ ) cycles. Thus,  $\beta$ -SnWO<sub>4</sub> is highly favorable to be utilized as an electrode material for energy storage devices.

**Author Contributions:** Data curation, V.V.; Formal analysis, M.S.; Investigation, V.V.; Methodology, H.N.S.; Project administration, F.A.A.; Resources, M.A.A.; Software, J.S.A.; Supervision, N.G.; Validation, M.S.J.; Writing—original draft, N.A.; Writing—review & editing, F.A.A. and N.G. All authors have read and agreed to the published version of the manuscript.

**Funding:** The authors thank the financial support from the Kingdom of Saudi Arabia, Ministry of Education, Najran University, Promising Centre for Sensors and Electronic Devices (PCSED) sanction on 2019 (Ref. No: PCSED-021-18). The researchers supporting project number (RSP-2020/160), King Saud University, Saudi Arabia. Nagaraju Ganganagappa thank DST Nanomission (Project No. SR/NM/NS-1262/2013 (G), New Delhi, Govt. of India for financial support to carry out the research work.

**Institutional Review Board Statement:** Not applicable.

**Informed Consent Statement:** Not applicable.

**Data Availability Statement:** Not applicable.

**Acknowledgments:** The authors thank the financial support from the Kingdom of Saudi Arabia, Ministry of Education, Najran University, Promising Centre for Sensors and Electronic Devices (PCSED) sanction on 2019 (Ref. No: PCSED-021-18). The researchers supporting project number (RSP-2020/160), King Saud University, Saudi Arabia. Nagaraju Ganganagappa thank DST Nanomission (Project No. SR/NM/NS-1262/2013 (G), New Delhi, Govt. of India for financial support to carry out the research work.

**Conflicts of Interest:** The authors declare no conflict of interest.

## References

1. Shinde, P.A.; Jun, S.C. Review on recent progress in the development of tungsten oxide based electrodes for electrochemical energy storage. *ChemSusChem* **2020**, *13*, 11–38. [[CrossRef](#)]
2. Hu, X.; Zhang, W.; Liu, X.; Mei, Y.; Huang, Y. Nanostructured Mo-based electrode materials for electrochemical energy storage. *Chem. Soc. Rev.* **2015**, *44*, 2376–2404. [[CrossRef](#)] [[PubMed](#)]
3. Zhang, N.; Xiao, X.; Pang, H. Transition metal (Fe, Co, Ni) fluoride-based materials for electrochemical energy storage. *Nanoscale Horizons* **2019**, *4*, 99–116. [[CrossRef](#)]
4. Borzutzki, K.; Thienenkamp, J.; Diehl, M.; Winter, M.; Brunklaus, G. Fluorinated polysulfonamide based single ion conducting room temperature applicable gel-type polymer electrolytes for lithium ion batteries. *J. Mater. Chem. A* **2019**, *7*, 188–201. [[CrossRef](#)]
5. Gao, B.; Li, X.; Ding, K.; Huang, C.; Li, Q.; Chu, P.K.; Huo, K. Recent progress in nanostructured transition metal nitrides for advanced electrochemical energy storage. *J. Mater. Chem. A* **2019**, *7*, 14–37. [[CrossRef](#)]
6. Wang, X.; Li, B.; Liu, D.; Xiong, H. ZnWO<sub>4</sub> nanocrystals/reduced graphene oxide hybrids: Synthesis and their application for Li ion batteries. *Sci. China Ser. B Chem.* **2013**, *57*, 122–126. [[CrossRef](#)]
7. Wang, P.; Liu, H.; Tan, Q.; Yang, J. Ruthenium oxide-based nanocomposites with high specific surface area and improved capacitance as a supercapacitor. *RSC Adv.* **2014**, *4*, 42839–42845. [[CrossRef](#)]
8. Shinde, P.A.; Lokhande, V.C.; Ji, T.; Lokhande, C.D. Facile synthesis of hierarchical mesoporous weirds-like morphological MnO<sub>2</sub> thin films on carbon cloth for high performance supercapacitor application. *J. Colloid Interface Sci.* **2017**, *498*, 202–209. [[CrossRef](#)]
9. Zhang, J.; Ding, J.; Li, C.; Li, B.; Li, D.; Liu, Z.; Liu, Y. Fabrication of novel ternary three-dimensional RuO<sub>2</sub>/graphitic-C<sub>3</sub>N<sub>4</sub>@reduced graphene oxide aerogel composites for supercapacitors. *ACS Sustain. Chem. Eng.* **2017**, *5*, 4982–4991. [[CrossRef](#)]
10. Prabakar, S.R.; Han, S.C.; Jeong, J.; Sohn, K.S.; Pyo, M. CoSn(OH)<sub>6</sub> hybridized with anionic and cationic graphenes as a new high-capacity anode for lithium ion batteries. *Mater. Des.* **2017**, *118*, 294–303. [[CrossRef](#)]
11. Prabakar, S.R.; Babu, R.S.; Oh, M.; Lah, M.S.; Han, S.C.; Jeong, J.; Pyo, M. Dense CoO/graphene stacks via self-assembly for improved reversibility as high performance anode in lithium ion batteries. *J. Power Sources* **2014**, *272*, 1037–1045. [[CrossRef](#)]
12. Manukumar, K.N.; Kishore, B.; Manjunath, K.; Nagaraju, G. Mesoporous Ta<sub>2</sub>O<sub>5</sub> nanoparticles as an anode material for lithium ion battery and an efficient photocatalyst for hydrogen evolution. *Int. J. Hydrogen Energy* **2018**, *43*, 18125–18135. [[CrossRef](#)]
13. Huang, B.; Li, X.; Pei, Y.; Li, S.; Cao, X.; Masse, R.C.; Cao, G. Novel carbon-encapsulated porous SnO<sub>2</sub> anode for lithium ion batteries with much improved cyclic stability. *Small* **2016**, *12*, 1945–1955. [[CrossRef](#)]
14. Liu, H.; Li, W.; Shen, D.; Zhao, D.; Wang, G. Graphitic carbon conformal coating of mesoporous TiO<sub>2</sub> hollow spheres for high-performance lithium ion battery anodes. *J. Am. Chem. Soc.* **2015**, *137*, 13161–13166. [[CrossRef](#)] [[PubMed](#)]
15. Zhu, G.; Que, W.; Zhang, J.; Zhong, P. Photocatalytic activity of SnWO<sub>4</sub> and SnW<sub>3</sub>O<sub>9</sub> nanostructures prepared by a surfactant-assisted hydrothermal process. *Mater. Sci. Eng. B* **2011**, *176*, 1448–1455. [[CrossRef](#)]
16. Ede, S.R.; Kundu, S. Microwave synthesis of SnWO<sub>4</sub> nanoassemblies on DNA scaffold: A novel material for high performance supercapacitor and as catalyst for butanol oxidation. *ACS Sustain. Chem. Eng.* **2015**, *3*, 2321–2336. [[CrossRef](#)]
17. Solis, J.L.; Lantto, V. Gas-sensing properties of different  $\alpha$ -SnWO<sub>4</sub>-based thick films. *Phys. Scripta* **1997**, *1997*, 281. [[CrossRef](#)]

18. Warmuth, L.; Feldmann, C.  $\beta$ -SnWO<sub>4</sub> with morphology-controlled synthesis and facet-depending photocatalysis. *ACS Omega* **2019**, *4*, 13400–13407. [[CrossRef](#)] [[PubMed](#)]
19. Cho, I.S.; Kwak, C.H.; Kim, D.W.; Lee, S.; Hong, K.S. Photophysical, photoelectrochemical, and photocatalytic properties of novel SnWO<sub>4</sub> oxide semiconductors with narrow band gaps. *J. Phys. Chem. C* **2009**, *113*, 10647–10653. [[CrossRef](#)]
20. Huang, R.; Ge, H.; Lin, X.; Guo, Y.; Yuan, R.; Fu, X.; Li, Z. Facile one-pot preparation of  $\alpha$ -SnWO<sub>4</sub>/reduced graphene oxide (RGO) nanocomposite with improved visible light photocatalytic activity and anode performance for Li-ion batteries. *RSC Adv.* **2012**, *3*, 1235–1242. [[CrossRef](#)]
21. Alharthi, F.A.; Alsaiani, M.A.; Jalalah, M.S.; Shashank, M.; Alghamdi, A.A.; Algethami, J.S.; Ganganagappa, N. Combustion synthesis of  $\beta$ -SnWO<sub>4</sub>-rGO: Anode material for Li-ion battery and photocatalytic dye degradation. *Ceram. Int.* **2020**, *47*, 10291–10300. [[CrossRef](#)]
22. Ansar, M.T.; Ali, A.; Mustafa, G.M.; Afzal, F.; Ishaq, S.; Kanwal, F.; Atiq, S. Polypyrrole-based nanocomposites architecture as multifunctional material for futuristic energy storage applications. *J. Alloy. Compd.* **2021**, *855*, 157341. [[CrossRef](#)]
23. Mustafa, G.M.; Atiq, S.; Abbas, S.K.; Riaz, S.; Naseem, S. Tunable structural and electrical impedance properties of pyrochlores based Nd doped lanthanum zirconate nanoparticles for capacitive applications. *Ceram. Int.* **2018**, *44*, 2170–2177. [[CrossRef](#)]
24. Pavithra, N.S.; Patil, S.B.; Kumar, S.K.; Alharthi, F.A.; Nagaraju, G. Facile synthesis of nanocrystalline  $\beta$ -SnWO<sub>4</sub>: As a photocatalyst, biosensor and anode for Li-ion battery. *SN Appl. Sci.* **2019**, *1*, 1123. [[CrossRef](#)]
25. Quader, A.; Mustafa, G.M.; Abbas, S.K.; Ahmad, H.; Riaz, S.; Naseem, S.; Atiq, S. Efficient energy storage and fast switching capabilities in Nd-substituted La<sub>2</sub>Sn<sub>2</sub>O<sub>7</sub> pyrochlores. *Chem. Eng. J.* **2020**, *396*, 125198. [[CrossRef](#)]
26. Garadkar, K.M.; Ghule, L.A.; Sapnar, K.B.; Dhole, S.D. A facile synthesis of ZnWO<sub>4</sub> nanoparticles by microwave assisted technique and its application in photocatalysis. *Mater. Res. Bull.* **2013**, *48*, 1105–1109. [[CrossRef](#)]
27. Han, L.; Zhou, X.; Wan, L.; Deng, Y.; Zhan, S. Synthesis of ZnFe<sub>2</sub>O<sub>4</sub> nanoplates by succinic acid-assisted hydrothermal route and their photocatalytic degradation of rhodamine B under visible light. *J. Environ. Chem. Eng.* **2014**, *2*, 123–130. [[CrossRef](#)]
28. Mani, S.; VEDIYAPPAN, V.; Chen, S.M.; Madhu, R.; Pitchaimani, V.; Chang, J.Y.; Liu, S.B. Hydrothermal synthesis of NiWO<sub>4</sub> crystals for high performance non-enzymatic glucose biosensors. *Sci. Rep.* **2016**, *6*, 24128. [[CrossRef](#)] [[PubMed](#)]
29. Ding, S.; Chen, J.S.; Lou, X.W. One-dimensional hierarchical structures composed of novel metal oxide nanosheets on a carbon nanotube backbone and their lithium-storage properties. *Adv. Funct. Mater.* **2011**, *21*, 4120–4125. [[CrossRef](#)]
30. Shim, H.W.; Cho, I.S.; Hong, K.S.; Lim, A.H.; Kim, D.W. Wolframite-type ZnWO<sub>4</sub> nanorods as new anodes for Li-ion batteries. *J. Phys. Chem. C* **2011**, *115*, 16228–16233. [[CrossRef](#)]
31. Patil, S.B.; Kishore, B.; Nagaraju, G.; Dupont, J. High capacity MoO<sub>3</sub>/rGO nanocomposite anode for lithium ion batteries: An intuition into the conversion mechanism of MoO<sub>3</sub>. *New J. Chem.* **2018**, *42*, 18569–18577. [[CrossRef](#)]
32. Kokulnathan, T.; Kumar, J.V.; Chen, S.M.; Karthik, R.; Elangovan, A.; Muthuraj, V. One-step sonochemical synthesis of 1D  $\beta$ -stannous tungstate nanorods: An efficient and excellent electrocatalyst for the selective electrochemical detection of antipsychotic drug chlorpromazine. *Ultrason. Sonochem.* **2018**, *44*, 231–239. [[CrossRef](#)] [[PubMed](#)]